

## Synthesis and electrochemical performance of porous carbon derived from medium and low temperature coal pitch

Shu Wang, Jinneng Wang\*

College of Civil Engineering and Architecture, Chongqing Institute of Engineering, Banan 400056, Chongqing, China

\*E-mail: [wangjn1985@163.com](mailto:wangjn1985@163.com)

Received: 3 October 2022 / Accepted: 23 November 2022 / Published: 27 December 2022

---

Porous activated carbon is widely used as electrode material for supercapacitors due to a series of characteristics such as its superior electrical conductivity, low preparation cost and no pollution to the environment, especially it has a good prospect in the application of electrode material for double layer supercapacitors. In this work, a series of porous carbon materials were prepared by KOH activation method using medium and low temperature coal pitch as raw material. Studies have shown that coal pitch contains a large number of hydrophilic functional groups such as -OH and -COOH and nitrogenous functional groups such as -NO<sub>2</sub>. The former can improve the dispersion of coal pitch in aqueous solution, while the latter can be used as a nitrogen precursor in the preparation of carbon materials. The results show that the porous carbon materials activated by KOH have the structural characteristics of coexistence of graphite microcrystals and amorphous carbon. The surface of the carbon material is rich in microporous structure and also has good electrochemical properties. The experimental results showed that the porous carbon exhibited excellent capacitive properties (210 F/g with 10.1 A/g) and good cycling stability under low temperature activation conditions at 500°C. In addition, the supercapacitor assembled from porous carbon has an energy density of 7.15 Wh/kg at a current density of 0.1A/g in 6 M KOH electrolyte.

---

**Keywords:** Coal pitch; Porous carbon; Supercapacitor; Electrochemical properties; Pore structure

### 1. INTRODUCTION

Due to the decline of oil reserves year by year and the increasing demand for oil and its downstream products in the daily life of human society, the worldwide oil shortage crisis will be inevitable in the future. Direct liquefaction of coal to oil technology is an important initiative to use the abundant coal resources to alleviate the shortage of oil resources [1,2]. The direct coal liquefaction process is a clean coal technology that converts organic matter in coal into liquid oil and chemicals through high-pressure hydrogenation and catalysis. However, under today's technology, the process

generates a large amount of residue regardless of the direct coal liquefaction technology or the solid-liquid separation method used [3,4]. Therefore, the research on the efficient classification and integrated utilization of coal direct liquefaction residue is an important issue for the development prospect of this technology. The direct coal liquefaction residue accounts for about 30% of the total raw coal and is mainly composed of unconverted coal organisms in the liquefied raw coal, inorganic minerals in the coal, additional liquefaction catalysts and some heavier coal liquefaction products [5]. The organic matter fractions in the direct coal liquefaction residue are mainly coal liquefaction heavy oil, asphaltene, preasphaltene and non-volatile fraction. One of the heavy oils enhances the fluidity of the coal direct liquefaction residue [6]. Asphaltene and preasphaltene fractions have a high degree of heavy and aromaticity, high bonding, high heat generation and inert non-volatile fraction content. The use of coal direct liquefaction residues as precursors for the production of high value-added carbon materials is a more economically efficient way to utilize coal direct liquefaction residues due to their high carbon content in asphaltene and their ease of polymerization and cross-linking. Xiao et al.[7] considered direct whipping residual of coal II flooding as supplementary foam carbon composite material. Hu et al.[8] took coal direct liquefaction residue as carbon precursor, and used chemical activation supplemented with template method to prepare graded pore carbon material, which has excellent electrochemical performance.

In the 1990s, Tateishi et al.[9] oxidized asphalt and other materials by  $\text{H}_2\text{SO}_4/\text{HNO}_3$  to obtain materials that are both uniformly dispersed in alkaline solutions and dissolved in partially polar organic solvents, and named them amphiphilic carbonaceous materials [10–12]. It was shown that the mixed acid oxidation process introduced a large number of hydrophilic functional groups, such as  $-\text{OH}$ ,  $-\text{COOH}$ ,  $-\text{NO}_2$ , and  $-\text{SOH}$ , to the edges of the thick-ringed macromolecules, which improved their hydrophilicity. However, the structure of the thick-ringed macromolecule itself is not completely destroyed after the oxidation treatment. Tateishi et al.[9] prepared gels by dissolving amphiphilic carbonaceous materials in ammonia and then directly after standing. This low-cost, green gel preparation method soon attracted the attention of researchers and was extended to catalyst carriers and other fields. Esumi et al. [13] prepared platinum-loaded carbon aerogels by mixing  $[\text{Pt}(\text{NH}_3)_4](\text{OH})_2$  with amphiphilic carbonaceous materials in aqueous solution, aging, drying, and charring. Thereafter, Wang et al.[14] prepared carbon-coated graphite by using amphiphilic carbonaceous materials as a carbon precursor and using its amphiphilic nature to coat graphite in aqueous solution, which showed excellent performance when used as a cathode material for lithium-ion batteries [15]. Subsequently, they prepared a mesoporous activated carbon with a mesoporous content of 26.9% and a specific surface area of 3347  $\text{m}^2/\text{g}$  by direct  $\text{KOH}$  activation of amphiphilic carbonaceous materials [16]. The material reached a mass specific capacitance of 348  $\text{F/g}$  and a volume specific capacitance of 163  $\text{F/cm}^3$  in the 6  $\text{MKOH}$  electrolyte system at a current density of 50  $\text{mA/g}$ . Guo et al.[17] prepared carbon-coated  $\text{Li}_4\text{Ti}_5\text{O}_{12}$  using amphiphilic carbonaceous materials as a carbon precursor, and the carbon-coating process greatly improved its performance when used as an electrode material for Li-ion batteries. In recent years, porous carbon materials such as activated carbon, mesoporous carbon, graded porous carbon and foam carbon have been considered as one of the most ideal electrode materials for supercapacitors because of their high specific surface area, excellent electrical conductivity, good stability and easily modulated surface chemistry [18]. At present, the preparation of porous carbon materials is mostly based on high-

temperature coal pitch, while there are fewer reports on the preparation of porous carbon materials based on medium- and low-temperature coal pitch. In this work, we investigated the pore structure and electrochemical properties of porous carbon materials at different activation temperatures using medium- and low-temperature coal pitch as the raw material.

## 2. EXPERIMENTAL

### 2.1. Chemicals

The medium and low temperature coal pitch (softening point 73.5 °C, coking value 26.22% was produced by Inner Mongolia Qinghua Group Co. Tridemethanol (99.5% GC) was purchased from Rohn Reagent. The p-toluenesulfonic acid, potassium hydroxide, hydrochloric acid, iodine, potassium iodide, soluble starch and sodium thiosulfate were purchased from Sinopharm Group.

### 2.2. Medium and low temperature coal pitch modification

The medium and low temperature coal pitch was modified by chemical cross-linking method with melamine as the cross-linking agent and p-toluenesulfonic acid as the catalyst. The coal asphalt was crushed and mixed with melamine and p-toluenesulfonic acid in a certain ratio into a three-necked flask, and then heated up to 100 °C at a rate of 5 °C/min, stirred for 30 min, continued to heat up to 160 °C, and then stirred for 3 h. The reaction was stopped and cooled to room temperature naturally, and the resulting product was the medium and low temperature coal pitch resin.

### 2.3. Preparation of porous carbon materials

The carbon precursors obtained by the above method were crushed and sieved. A certain amount ( $D < 200 \mu\text{m}$ ) of the precursor was weighed and transferred into a tube furnace and heated to 500 °C under nitrogen atmosphere at a rate of 5 °C/min and charred at a constant temperature for 40 min. After cooling to room temperature, the sample was removed and labeled as BC. BC and KOH were weighed in a mass ratio of 1:2, and BC-500 was impregnated in KOH solution (1 g KOH dissolved in 1 mL water). After 12 h, the excess water was evaporated and transferred to a tube furnace, which was heated to the set temperature (600, 700, 800°C) at a rate of 5 °C/min under nitrogen atmosphere. The samples were cooled naturally to room temperature after 1 h of constant temperature. The activated samples were acid washed and washed with water to reach pH 7, and then dried to obtain the finished porous carbon, which was recorded as BC-x, x representing different activation temperatures.

### 2.4. Material characterization

The sample microstructure was analyzed by X-ray diffractometer and Raman spectroscopy. The XRD scan range is 10 ~90° with a step size of 0.02°. The Raman incident wavelength is 532 nm and the

wave number ranges from 500 to 2500 cm. The pore structure of the samples was measured by gas adsorption analyzer, the specific surface area was calculated according to BET theory, and the pore parameters and pore size distribution were calculated according to density functional theory DFT method.

### 2.5. Electrode preparation

The preparation process of electrodes plays an important role in the characterization of material properties, and the following process is used to prepare electrodes in this thesis: weigh a certain amount of active substance and add a small amount of ethanol to wet it. Add the binder and conductive agent in the ratio of  $m(\text{active substance}):m(\text{conductive carbon black}):m(\text{polytetrafluoroethylene}) = 85:10:5$ . Mix the above substances well to obtain a viscous slurry. After stirring until the paste is semi-dry, it is rolled into a thin carbon sheet of uniform thickness by a series press, and then cut into round carbon sheets with a diameter of 8 mm by a hole punch. The charcoal was dried under vacuum at 100 °C to a constant weight, and the charcoal flakes with a mass of 4.0-5.5 mg were then prepared. The dried charcoal pieces with a mass between 4.0 and 5.5 mg were pressed between two circular nickel foam collectors by a spinning press, using nickel wire as the electrode lug. The prepared electrodes were vacuum-impregnated in 6 MKOH electrolyte for 24 h before testing.

### 2.6. Electrochemical characterization

The three-electrode system was assembled with 6 M potassium hydroxide solution as the electrolyte, porous carbon electrode as the working electrode, Pt electrode as the counter electrode and Hg/HgO electrode as the reference electrode. Cyclic voltammetry (CV), constant current charging and discharging (GCD), and electrochemical impedance spectroscopy (EIS) tests were performed using an electrochemical workstation. The cyclic voltammetry was performed at voltages from - 1 to 0 V with scan rates of 5, 10, 30, 50, 70, 90, and 100 mV/s. The constant-current charging and discharging was performed at voltages from 0 to 1 V and current densities from 0.5 to 10.0 A/g. The frequency range of the AC impedance was from 0.01 Hz to 100 kHz with an amplitude of 5 mV.

## 3. RESULTS AND DISCUSSION

To study the changes of asphalt, infrared spectra of asphaltene and BC were analyzed. The infrared spectra of asphaltene and BC are shown in Figure 1. It can be seen from the figure that in the preparation of BC from asphaltene, the original absorption peaks of asphaltene are retained to a certain extent. The absorption peak located around  $3434\text{ cm}^{-1}$  is attributed to the stretching vibration of the O-H bond in the hydroxyl group. The absorption peak located near  $2924\text{ cm}^{-1}$  is attributed to the stretching vibration of the saturated C-H bond at the edge of the thick ring in asphaltene [19,20]. The strong absorption peak located around  $1622\text{ cm}^{-1}$  is attributed to the stretching vibration of the aromatic ring

backbone. The absorption peak located around  $1039\text{ cm}^{-1}$  corresponds to the symmetric stretching vibration of the O-S-O bond of the sulfonic acid group. This is mainly due to the small amount of sulfur contained in the asphaltene extracted from BC. However, a new absorption peak also appears in BC, and the absorption peak located around  $1722\text{ cm}^{-1}$  is attributed to the C=O symmetric stretching vibration of the carboxyl group [21–23]. This indicates the introduction of some carboxyl groups at the edges of the mixed aromatic compounds. The absorption peaks located around  $1538\text{ cm}^{-1}$  and  $1345\text{ cm}^{-1}$  are attributed to the symmetric and asymmetric stretching vibrations of nitro [24,25]. This indicates that aromatic compounds undergo nitration reactions to convert aromatic compounds to nitroaromatics [26]. The absorption peak located around  $1258\text{ cm}^{-1}$  corresponds to the C-O and H-O stretching vibrations of the carboxyl group. In addition, the symmetric stretching vibration ( $1380\text{ cm}^{-1}$ ) absorption peak belonging to the aryl cycloalkyl branched chain in BC disappears, which may be due to the fact that the thick ring aromatic with branched chain is easily oxidized by strong oxidants and converted to carboxylic acid [27].

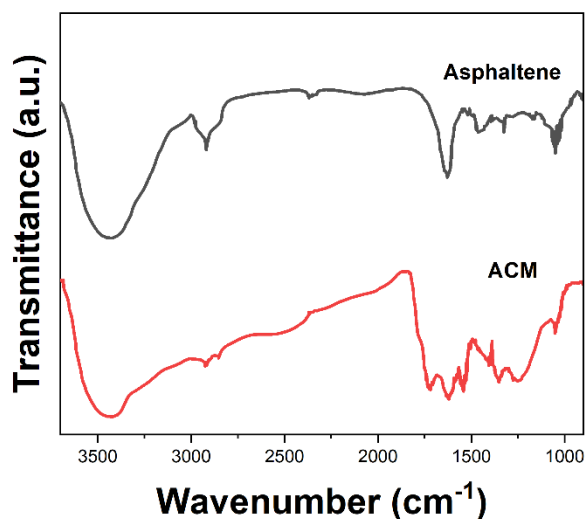


**Figure 1.** FTIR spectra of bitumen and prepared BC.

Figure 2 shows the XRD spectra of porous carbon materials at BC and different activation temperatures. From Figure 2, two diffraction peaks appear near  $25^\circ$  and  $44^\circ$  in BC, which represent the (002) and (100) crystal plane diffraction of graphite microcrystals, respectively. The peak at (002) of BC-600 is sharper, indicating a relatively high degree of order [28]. Compared with BC, the intensity of the peaks at (002) and (100) of the activated porous carbon material was weakened. This indicates that the degree of ordering of the samples was reduced due to the disruption of the graphitized structure of the porous carbon after KOH activation, which led to the transformation of the stacking structure of the aromatic layer to an amorphous structure [29], resulting in the increase of pores, and this phenomenon was more obvious with the increase of the activation temperature [30].

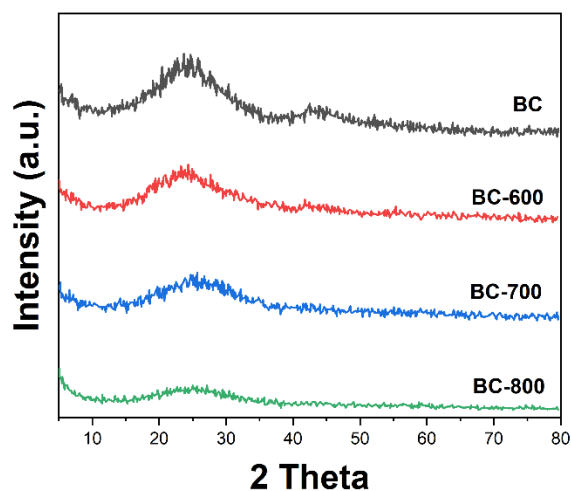


**Figure 2.** XRD patterns of BC, BC-600, BC-700 and BC-800.

In order to further characterize the degree of graphitization of porous carbon, Raman spectroscopy was performed on BC and porous carbon materials (Figure 3). All samples showed two characteristic absorption peaks, D and G, near  $1355\text{ cm}^{-1}$  and  $1600\text{ cm}^{-1}$  [31]. The D peak is related to the degree of crystal defects or disordering of the carbon material, while the G peak is related to the degree of graphitization of the carbon material. The intensity ratio of the D and G peaks is generally used to measure the degree of disorder and defects in carbon materials [32]. The smaller the value of  $I_D/I_G$ , the higher the degree of graphitization and the lower the degree of disorder. On the contrary, the graphitization is low and disordering is high. The  $I_D/I_G$  values of BC and porous carbon materials were obtained by Raman spectroscopy split-peak fitting [33–35]. The lowest  $I_D/I_G$  value of unactivated BC was 3.66. The  $I_D/I_G$  values of porous carbon materials increased and then decreased with the increase of activation temperature, and the  $I_D/I_G$  values of BC-600, BC-700 and BC-800 were 4.15, 4.29 and 4.39, respectively. The  $I_D/I_G$  values of all porous carbons are greater than BC. This is due to the destruction of the graphitized structure of the porous carbons by the etching effect of KOH [36,37]. Due to the erosion process of KOH, the stacking structure of the aromatic layer changed to an amorphous structure, resulting in a gradual increase of the  $I_D/I_G$  value [38,39]. The microcrystalline structure of the prepared porous carbon is amorphous carbon and contains some graphite microcrystals [40].

The  $\text{N}_2$  adsorption isotherms and pore size distribution curves of BC, BC-600, BC-700 and BC-800 are shown in Figure 4. It can be seen from Figure 4A that the BC is mainly a microporous structure. The main feature of the adsorption isotherm is the presence of a steep increase in adsorption at low relative pressures, followed by a plateau [41]. The amount of adsorption increases slightly when the relative pressure approaches 1.0. This is mainly due to the partial macroporous structure formed between the particles. And BC-600, BC-700 and BC-800 all show similar types of adsorption isotherms.

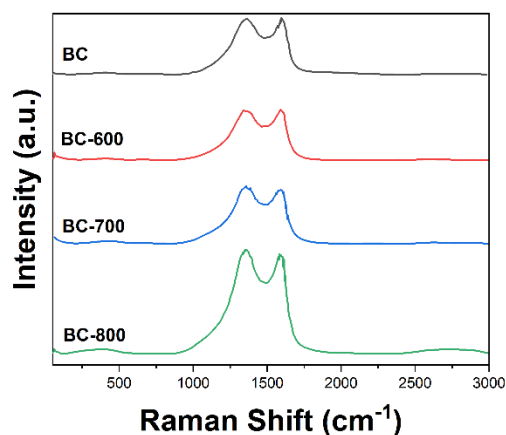


**Figure 3.** Raman spectra of BC, BC-600, BC-700 and BC-800.

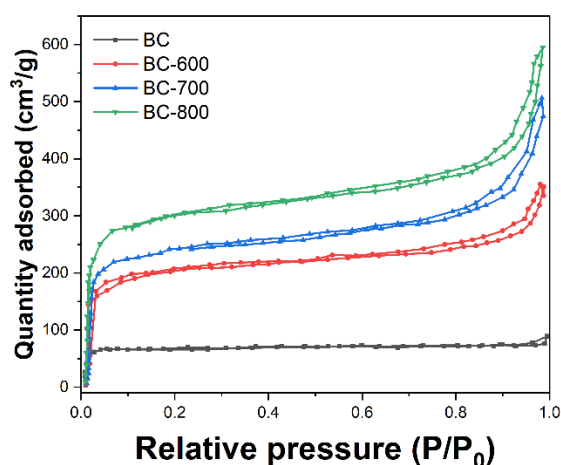


**Figure 4.** Nitrogen sorption isotherms of BC, BC-600, BC-700 and BC-800.

The main feature is the existence of a steep increase in adsorption at lower relative pressures, indicating that the materials all have a certain amount of microporosity [42]. A wide hysteresis loop exists in the relative pressure range of 0.45 to 1.0, and the hysteresis loop is more pronounced at higher relative pressures. This indicates the presence of mesopores in the material with relatively large pore sizes [43]. The increase in adsorption at relative pressures close to 1.0 indicates the presence of some macroporosity. The pore size distribution curves in Figure 4B also show that BC is mainly a microporous structure, while BC-600, BC-700 and BC-800 have some microporous, mesoporous and macroporous distribution.

Figure 5A shows the cyclic voltammetry curves of BC, BC-600, BC-700 and BC-800 at 10 mV/s. We can see that in the potential window of -0.8-0V, the CV curves of BC-600 and BC-700 exhibit a rectangular shape and have distinct redox peaks [42,44]. When the KOH activation temperature is 800 °C, the redox peak in the BC-800 CV curve has completely disappeared. Also, the hump-like CV curve

shape was not found in the BC samples. the pseudocapacitance generated in the BC-600 and BC-700 materials may be generated by the Faraday redox reaction [45].

The GCD curves of BC, BC-600, BC-700 and BC-800 at a current density of 1A/g are shown in Figure 5B. It is obvious that the GCD curve of BC exhibits a shape similar to isosceles triangle. From the discharge curves, it can be seen that the discharge time of BC-600, BC-700 and BC-800 is significantly longer than that of BC, so the specific capacitance is significantly higher than that of the BC sample [46]. According to the formula, the order of the specific capacitance is calculated as BC-600 > BC-700 > BC-800 > BC.

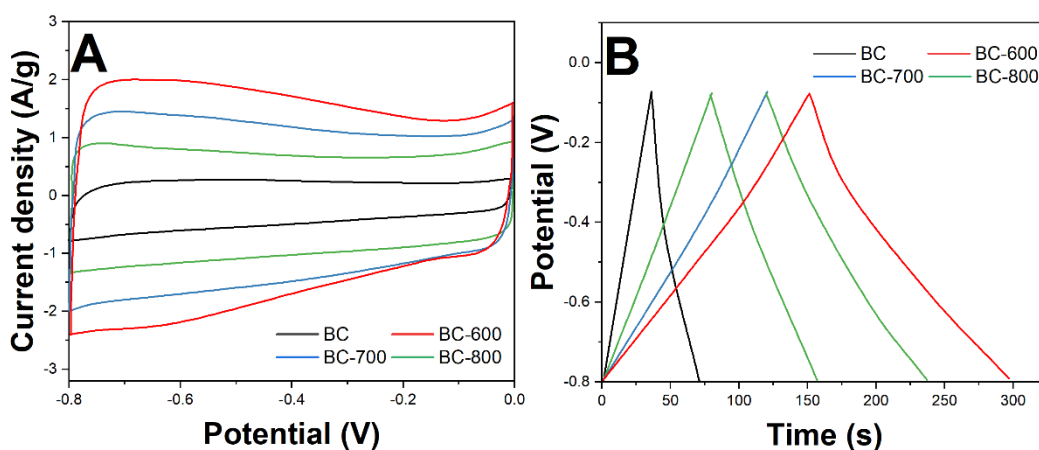


**Figure 5.** (A) CV curves and (B) GCD curves of BC, BC-600, BC-700 and BC-800 at scan rate of 10 mV/s with 1 mA/g.

Figure 5A shows the Nyquist plots of BC, BC-600, BC-700 and BC-800. The inset shows the equivalent circuit model fit. The intercept on the real axis in the high frequency region represents the internal resistance ( $R_s$ ) of the material, which can be derived from the fact that all BC materials have a very small internal resistance [43]. The low internal resistance is very beneficial to the energy storage and conversion of the supercapacitor. The internal resistance of BC600, BC-700, and BC-800 is 0.65, 0.63, and 0.76  $\Omega$ , respectively. This fully demonstrates the excellent electrical conductivity of BC after activation. In the high frequency region of the impedance spectrum [47], semicircular rings (the size of the semicircular diameter represents the charge transfer resistance- $R_{ct}$ , the smaller the diameter of the semicircle, the lower the charge transfer resistance) appear, with semicircular ring diameters of 1.46, 0.27, 0.28 and 0.29  $\Omega$  for BC, BC-600, BC-700 and BC-800, respectively. This further indicates that the BC material has a very low charge transfer resistance and therefore possesses fast charge transfer capability and good conductivity, and exhibits good power density for supercapacitor applications. The slope of the 45° portion of this curve at intermediate frequencies is known as the Warburg resistance ( $Z_w$ ). This is caused by the diffusion/transport of ions in the electrolyte to the electrode surface. In the low frequency region, the samples all exhibit almost vertical straight lines, which collectively indicate

that BC possesses ideal double-layer capacitive behavior as an electrode material for supercapacitors [48].

We further investigated the multiplicative performance of the N-CNS material, and Figure 5B depicts the specific capacitance versus current density for current densities between 0.1 - 20 A/g. From the figure, it can be seen that the specific capacitance of the material decays with the increase of current density, but the decay of the specific capacitance of the material is small at high currents [49,50]. In summary, it shows that the BC-600 material is very suitable as the electrode material for supercapacitor.

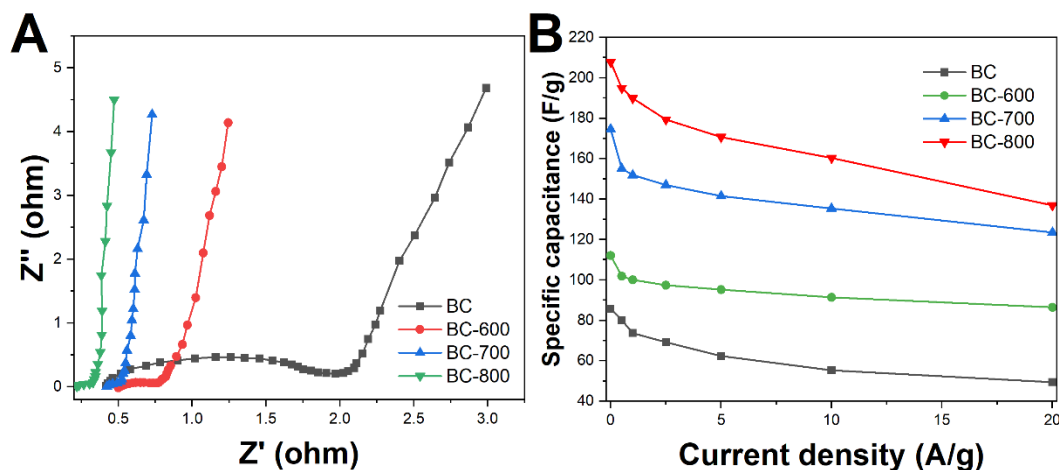


**Figure 5.** (A) Nyquist plots and (B) specific capacitance to current density of BC, BC-600, BC-700 and BC-800.

Figure 6A shows the CV curves of the BC-600 at different scan rates. It is clear that the CV curves show a certain degree of distortion as the scan rate increases from 5 mV/s to 100 mV/s, but still maintain a good quasi-rectangular shape. This indicates that the electrolyte ions still exhibit a fast ion response at higher scan rates. This further indicates that the material has good multiplicity when used as an electrode material for supercapacitors [51].

The constant-current charge/discharge curves of BC-600 at different current densities are shown in Figure 6B. From Figure 6B, it can be seen that the charge/discharge curves maintain very good symmetry as the specific capacity value of the electrode material decreases with the increase of current density. This indicates that the reversible performance of the sample remains good as the current density increases. From the calculations we can conclude that the symmetric capacitor assembled from BC-600 has an energy density of 7.15 Wh/kg at a current density of 0.1 A/g for an operating potential window of 0-1 V, corresponding to a power density of 50.4 W/kg. This data value can be compared to the energy density data of most carbon-based supercapacitors and many porous carbon materials. Compared with related references (Table 1), it can be found that the BC-600 in this work has a competitive specific capacitance and power storage performance.

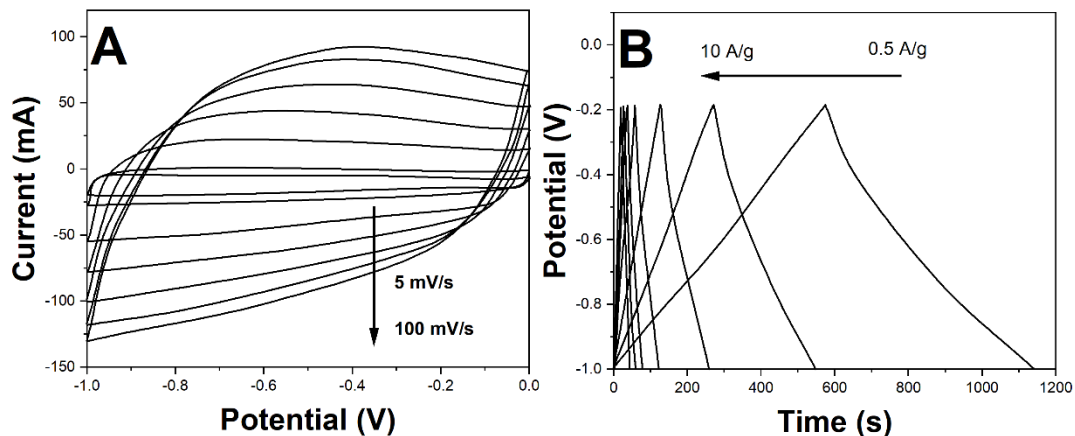


**Figure 6.** (A) CV and (B) GCD curves of BC-600 at different scanning rates and current densities.

**Table 1.** The comparison of the capacity performances of BC-600 with references.

Material	Electrolyte	Current density (A/g)	Specific capacitance (F/g)	Reference
Porous Carbon	6 M KOH	1.0	333	[52]
NiFe <sub>2</sub> O <sub>4</sub> Nanosheets	6 M KOH	1.0	377	[53]
Porous Carbon	6 M KOH	1.0	269	[54]
BC-600	6 M KOH	0.1	251	This work

#### 4. CONCLUSION

In this work, medium- and low-temperature coal pitch-based porous carbon was produced on a large scale by a simple, low-cost method. The prepared porous carbon materials possess a high specific surface area. In addition, the BC-600 electrode materials were assembled into symmetric supercapacitors in 6M KOH solution, exhibiting a high energy density of 7.15 Wh/kg and very good cycling stability. the BC-600 contact resistance is small and the curve is almost perpendicular to the real axis in the low frequency region, indicating its good capacitive properties. This method, which facilitates the synthesis of porous carbon on a large scale and at low cost, can meet the capacitive energy storage devices in practical applications.

#### ACKNOWLEDGMENTS

This work was supported by Foundation of Chongqing Institute of Engineering (No.2021xzky09) and Foundation of Chongqing Institute of Engineering (No.2021gcky01).

#### References

1. Q. Huang, X. Li, G. Zhang, Y. Kan, C. Li, J. Deng, C. Wang, *Appl. Energy*, 309 (2022) 118434.
2. X. Yang, Z. Zhang, Z. Cai, Y. Chen, *Appl. Therm. Eng.*, 213 (2022) 118748.

3. B. Joshi, E. Samuel, Y. Kim, A.L. Yarin, M.T. Swihart, S.S. Yoon, *Chem. Eng. J.*, 430 (2022) 132876.
4. M.K. Rogachev, T. Nguyen Van, A.N. Aleksandrov, *Energies*, 14 (2021) 5016.
5. J. Weng, Q. Huang, X. Li, G. Zhang, D. Ouyang, M. Chen, A.C.Y. Yuen, A. Li, E.W.M. Lee, W. Yang, J. Wang, X. Yang, *Energy Storage Mater.*, 53 (2022) 580–612.
6. A. Guo, F. Wang, S. Jiao, U.-K. Ibrahim, D. Liu, H. Liu, K. Chen, Z. Wang, *Fuel*, 276 (2020) 118037.
7. N. Xiao, Y. Zhou, J. Qiu, Z. Wang, *Fuel*, 89 (2010) 1169–1171.
8. J. Zhang, L. Jin, J. Cheng, H. Hu, *Carbon*, 55 (2013) 221–232.
9. D. Tateishi, K. Esumi, H. Honda, *Carbon*, 29 (1991) 1296–1298.
10. Q. Zhao, X. Tan, T. Ma, F. Cao, Z. Xia, H. Liu, H. Ning, Z. Li, H. Hu, M. Wu, *J. Colloid Interface Sci.*, 587 (2021) 810–819.
11. R. Tabassam, F. Alvi, N. Aslam, R. Raza, Saifur-Rehman, L. Sherin, M. Ajaml, A. Ali, *Mater. Lett.*, 302 (2021) 130275.
12. J. Lu, M. Cheng, C. Zhao, B. Li, H. Peng, Y. Zhang, Q. Shao, M. Hassan, *Ind. Crops Prod.*, 176 (2022) 114267.
13. K. Esumi, R. Ono, H. Sugii, H. Honda, M. Kodama, *Colloids Surf. Physicochem. Eng. Asp.*, 94 (1995) 93–96.
14. J. Wang, M. Chen, C. Wang, B. Hu, J. Zheng, *Mater. Lett.*, 64 (2010) 2281–2283.
15. Y. Zhu, Y. Wang, C. Gao, W. Zhao, X. Wang, M. Wu, *New Carbon Mater.*, 35 (2020) 358–370.
16. J. Wang, M. Chen, C. Wang, J. Wang, J. Zheng, *J. Power Sources*, 196 (2011) 550–558.
17. X. Guo, C. Wang, M. Chen, J. Wang, J. Zheng, *J. Power Sources*, 214 (2012) 107–112.
18. J.-G. Wagenfeld, K. Al-Ali, S. Almheiri, A.F. Slavens, N. Calvet, *Waste Manag.*, 95 (2019) 78–89.
19. D. Wang, L. Xu, J. Nai, T. Sun, *J. Alloys Compd.*, 786 (2019) 109–117.
20. R. Tu, Y. Sun, Y. Wu, X. Fan, J. Wang, S. Cheng, Z. Jia, E. Jiang, X. Xu, *Renew. Energy*, 167 (2021) 82–90.
21. X. Zhou, T.B. Moghaddam, M. Chen, S. Wu, S. Adhikari, *Sci. Total Environ.*, 745 (2020) 141096.
22. J. Feng, J. Feng, H.M. Loussala, S. Han, X. Ji, C. Li, H. Sun, M. Sun, *Food Chem.*, 364 (2021) 130379.
23. H. Javed, D.X. Luong, C.-G. Lee, D. Zhang, J.M. Tour, P.J.J. Alvarez, *Carbon*, 140 (2018) 441–448.
24. M. Kamran, M. Dauda, C. Basheer, M.N. Siddiqui, H.K. Lee, *J. Chromatogr. A*, 1631 (2020) 461559.
25. X. Hu, K. Dai, P. Pan, *J. Clean. Prod.*, 209 (2019) 1484–1493.
26. W. Yang, C. Wang, B. Jiang, R. Li, H. Bai, N. Ta, S. Du, C. Zhang, Z. Li, X. Wang, Y. Li, *Carbon*, 200 (2022) 390–400.
27. C. Zhang, D. Li, Y. Xie, D. Stalla, P. Hua, D.T. Nguyen, M. Xin, J. Lin, *Fuel*, 290 (2021) 120080.
28. L. Chen, J. Xu, Q. Hasi, Y. Zhang, X. Jiang, L. Zhang, K. Xu, L. Li, A. Li, *Sep. Purif. Technol.*, 286 (2022) 120453.
29. Y. Liu, X. Qin, S. Zhang, Y. Huang, F. Kang, G. Chen, B. Li, *Energy Storage Mater.*, 18 (2019) 320–327.
30. Y. Wang, J. Chen, H. Ihara, M. Guan, H. Qiu, *TrAC Trends Anal. Chem.*, 143 (2021) 116421.
31. Y. Zhang, G. Ji, C. Li, X. Wang, A. Li, *Chem. Eng. J.*, 390 (2020) 124398.
32. C. Wang, H. Wang, B. Dang, Z. Wang, X. Shen, C. Li, Q. Sun, *Renew. Energy*, 156 (2020) 370–376.
33. H. Yuan, J. Chen, D. Li, H. Chen, Y. Chen, *Chem. Eng. J.*, 373 (2019) 171–178.
34. H. Zhao, Y. Cheng, Z. Zhang, B. Zhang, C. Pei, F. Fan, G. Ji, *Carbon*, 173 (2021) 501–511.
35. X. Zhou, Z. Jia, X. Zhang, B. Wang, W. Wu, X. Liu, B. Xu, G. Wu, *J. Mater. Sci. Technol.*, 87 (2021) 120–132.
36. H. He, Y. Wang, Z. Zhao, Q. Wang, Q. Wei, Y. Cai, *J. Energy Storage*, 55 (2022) 105358.

37. Y. Sun, Y. Liu, Y. Han, Z. Li, G. Ning, R. Xing, X. Ma, *Mater. Today Commun.*, 29 (2021) 102982.
38. J. Luo, C. Jia, M. Shen, S. Zhang, X. Zhu, *Carbon*, 155 (2019) 403–409.
39. L. Guan, L. Pan, T. Peng, T. Qian, Y. Huang, X. Li, C. Gao, Z. Li, H. Hu, M. Wu, *Carbon*, 152 (2019) 537–544.
40. C. Su, Y. Guo, L. Yu, J. Zou, Z. Zeng, L. Li, *Mater. Chem. Phys.*, 258 (2021) 123930.
41. J. Zheng, B. Yan, L. Feng, Q. Zhang, C. Zhang, W. Yang, J. Han, S. Jiang, S. He, *Diam. Relat. Mater.*, 128 (2022) 109247.
42. T. Bi, H. Chen, J. Li, X. Zhang, Q. Lin, *Electrochimica Acta*, 433 (2022) 141266.
43. G. Zhang, F. Yang, X. Liu, H. Zhao, S. Che, J. Li, X. Yan, S. Sun, F. Chen, C. Xu, H. Liu, Q. Wei, Y. Li, *Sep. Purif. Technol.*, 280 (2022) 119923.
44. L. Chai, P. Wang, X. Liu, Y. Sun, X. Li, J. Pan, *J. Power Sources*, 532 (2022) 231324.
45. Y. Liu, L. Li, Z. Duan, Q. You, G. Liao, D. Wang, *Colloids Surf. Physicochem. Eng. Asp.*, 610 (2021) 125728.
46. E.-K. Kim, B.-M. Lee, J.-J. Park, J.-H. Choi, J.M. Yun, *Mater. Today Sustain.* (2022) 100238.
47. C. Liang, J. Chen, K. Yu, W. Jin, *J. Alloys Compd.*, 878 (2021) 160445.
48. Y. Wang, X. Bai, W. Wang, Y. Lu, F. Zhang, B. Zhai, X. Wang, Y. Song, *J. Energy Storage*, 38 (2021) 102496.
49. L. Hou, W. Yang, B. Jiang, P. Wang, L. Yan, C. Zhang, G. Huang, F. Yang, Y. Li, *Carbon*, 183 (2021) 176–186.
50. L. Hou, W. Yang, Y. Li, P. Wang, B. Jiang, C. Xu, C. Zhang, G. Huang, F. Yang, Y. Li, *Chem. Eng. J.*, 417 (2021) 129289.
51. Y. Zhang, R. Shao, W. Xu, J. Ding, Y. Wang, X. Yan, W. Shi, M. Wang, *Chem. Eng. J.*, 419 (2021) 129576.
52. X. Jiang, *Int J Electrochem Sci*, 17 (2022) 2.
53. J. Chen, F. Zhang, Z. Li, X. Ren, S. Han, M. Cai, H. Gao, L. Li, *Int J Electrochem Sci*, 17 (2022) 220942.
54. F. Yu, F. Wang, Y. Yang, *Int J Electrochem Sci*, 17 (2022) 221059.